Numerical study of transonic cavity flows using large-eddy and detached-eddy simulation

P. Nayyar
CFD Laboratory
Department of Aerospace Engineering
University of Glasgow
Glasgow, UK

G. N. Barakos and K. J. Badcock
Department of Engineering
University of Liverpool
Liverpool, UK

ABSTRACT

Numerical analysis of the flow in weapon bays modelled as open rectangular cavities of length-to-depth (L/D) ratio of 5 and width-to-depth (W/D) ratio of 1 with doors-on and doors-off is presented. Flow conditions correspond to Mach and Reynolds numbers (based on cavity length) of 0·85 and 6·783m respectively. Results from unsteady Reynolds-averaged Navier-Stokes (URANS), large-eddy simulation (LES) and detached-eddy simulation (DES) are compared with the simulation methods demonstrating the best prediction of this complex flow. It was found that URANS was not able to predict the change of flow characteristics between the doors-on and doors-off configurations. In addition, the energy content of the cavity flow modes was much better resolved with DES and LES. Further, the DES was found to be quite capable for this problem giving accurate results (within 3dB of) experiments and appears to be a promising alternative to LES for modelling massively separated flows.

NOMENCLATURE

a, b	arbitrary parameters
C_{DES}	DES coefficient
C_{w1}, f_{w1}	closure coefficients for the one-equation Spalart-Allmaras model
d, $\tilde{d}$	distance to nearest wall
DES	detached eddy simulation
F_1	blending function used in the SST model
F_2	vorticity-dependent shear stress limiter for the SST model
k	turbulent kinetic energy
L/D	length-to-depth ratio
LES	large-eddy simulation
p_{rms}	root mean square pressure
SGS	sub-grid scale
SPL	sound pressure level
UCAV	uninhabited combat aerial vehicle
URANS	unsteady Reynolds-averaged Navier Stokes
W/D	width-to-depth ratio$y$
y_n	distance normal to wall
α, ß, β^*, σ_k, σ_ω	k-ω model coefficients
ε	turbulent dissipation rate
ν	kinematic viscosity
$\tilde{\nu}$	undamped eddy viscosity
ω	turbulent dissipation rate specific to turbulent kinetic energy
Δ	grid size metric

1.0 INTRODUCTION

Modern high performance aircraft carry stores placed inside cavities embedded in the aircraft's fuselage. Consequently, during the store release phase of operation the aircraft will have to fly with the cavities

Paper No. 2968. Manuscript received 29 March 2005, revised 25 April 2006, accepted 13 November 2006.

exposed to the free-stream of air. During this phase, an unsteady, highly energetic flow-field develops inside the cavity causing structural, acoustic and aerodynamic problems. Unsteady cavity flows, which represent aircraft weapon bays, have been investigated by Rossiter[1] in the 1960s at the Royal Aircraft Establishment. The understanding of cavity flow aerodynamics obtained by Rossiter's experiments was adequate for alleviating most of the problems encountered in the aircraft of that time. Recent designs, however, operate at extreme conditions and have additional requirements for quieter operation and more lightweight structures. For this reason, the cavity flow problem is now re-visited by aerospace engineers to develop a better understanding of this complex flow and to improve the current design methods. Furthermore, modern high-speed aircraft require more effective store carriage methods, especially at supersonic speeds, and internal store is put forward as an alternative to external wing and fuselage-mounted pylons. It is however recognised that the internal carriage of missiles can be affected by large flow perturbations in the vicinity of the weapon bay, through which the missile must traverse during launch. Most efforts undertaken to understand the separation and release characteristics of stores involved experiments[2] conducted at supersonic speeds and for shallow cavities with high aspect ratios. Although deeper cavities with low length-to-depth ratios (L/D) are known to exhibit more benign store release characteristics, the presence of the store can still influence the flow-field and hence alter the store release and separation characteristics. With uninhabited combat aerial vehicles (UCAVs) likely to play a significant part in future military aircraft designs, store release at transonic speeds and with deeper weapons bays is still plausible.

In view of the above, accurate CFD predictions of clean cavity flows are important before more complex configurations including store release can be tackled. Some current research has looked at the simulation of cavity flows via methods such as large-eddy simulation (LES)[3]. LES works by filtering the flow structures in terms of scale size, with the larger scales explicitly resolved and the much smaller ones modelled using a sub-grid scale (SGS) model. With a significantly lower proportion of the flow modelled compared to unsteady Reynolds-averaged Navier-Stokes (URANS) methods, LES solutions are potentially more useful. For high Reynolds number flows, however, LES is expensive. Recent endeavours have therefore looked at developing hybrids of URANS and LES to obtain the best of both methods. One example of such developments includes detached-eddy simulation (DES), as was introduced by Spalart[4] and which is now currently available in many CFD solvers.

This work focuses on how CFD can be used for the analysis of the flow-field inside a weapons bay, building on the experiments performed by Ross of QinetiQ[5]. The experiment considered a clean, open rectangular cavity with a length-to-depth ratio (L/D) of 5 and a width-to-depth ratio (W/D) of 1 with doors-on and doors-off. The flow conditions correspond to a Mach number of 0·85 and a Reynolds number of 6·783m based on the cavity length. A variety of turbulence modelling and simulation techniques have been used, including LES and DES. Computations have been performed with the parallel multi-block (PMB) code developed at the University of Glasgow[6]. Results are presented from URANS, LES and DES methods for both doors-off and doors-on cavity configurations. Comparisons were made with unsteady pressure measurements at the cavity floor[5] and with PIV measurements[7], and are discussed in detail in the following sections.

2.0 MATHEMATICAL MODEL

2.1 CFD solver

The parallel multi-block (PMB) flow solver[6] solver has been successfully applied to a variety of problems including cavity flows, hypersonic film cooling, spiked bodies, flutter and delta wing flows amongst others. The code solves the unsteady Reynolds averaged Navier-Stokes (RANS) equations on multi-block structured grids, in serial or parallel mode.

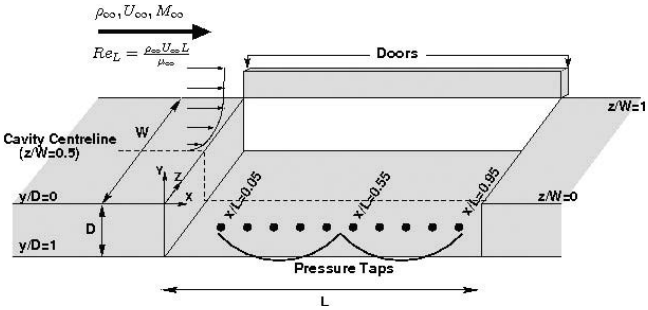

Figure 1. A schematic of the 3D, L/D = 5, W/D = 1 cavity (with doors-on) illustrating the positions of the pressure taps at which experimental and numerical results were compared.

Governing equations are discretised using a cell-centred finite volume method. The convective terms are discretised using either Osher's or Roe's scheme. MUSCL interpolation is used to provide nominally third order accuracy and the Van Albada limiter is used to avoid spurious oscillations across shocks. The time-marching of the solution is based on an implicit, dual time-stepping method. The final algebraic system of equations is solved using a conjugate gradient method, in conjunction with block incomplete lower-upper factorisation. A number of turbulence models including one and two-equation statistical models as well as large-eddy simulation (LES) and detached-eddy simulation (DES) formulations have been implemented into the code. At the moment, the standard Smagorinsky sub-grid scale (SGS) model is used for LES while the one-equation Spalart-Allmaras and the two-equation k-ω and SST turbulence models are available for DES.

2.2 Turbulence modelling

The SST turbulence model is typically presented as a 'blend' of the k-ω/k-ε models[8] but is phrased in k-ω form in PMB. The blended values for the model coefficients $\alpha, \beta, \sigma_k^{-1}$ and σ_ω^{-1} are given by

$$B\begin{pmatrix} a \\ b \end{pmatrix} \equiv F_1 a + (1 - F_1) b \qquad \ldots (1)$$

The blending function is defined as

$$F_1 = \mathrm{Tan}h(\mathrm{Arg}_1^4),$$
$$\mathrm{Arg}_1 = \min\left[\max\left(\frac{k^{1/2}}{\beta^* \omega y}, \frac{500\nu}{y_n^2 \omega}\right), \frac{2k\omega}{y_n^2 \max(\nabla k \cdot \nabla \omega, 0)}\right] \qquad \ldots (2)$$

The SST model places an additional vorticity-dependent limiter on the shear stress, which is denoted as F_2:

$$F_2 = \mathrm{Tan}h(\mathrm{Arg}_2^2),$$
$$\mathrm{Arg}_2 = \max\left(\frac{2k^{1/2}}{\beta^* \omega y}, \frac{500\nu}{y^2 \omega}\right) \qquad \ldots (3)$$

2.3 DES formulation

Spalart[4] modified the one-equation Spalart-Allmaras model to achieve a DES equivalent. The only modification is in the dissipation term of the transport equation of $\tilde{\nu}$, given as

$$-C_{w1} f_{w1} \left(\frac{\tilde{\nu}}{\tilde{d}}\right)^2 \qquad \ldots (4)$$

Originally,

$d = \tilde{d}$ is the distance of the nearest wall. $\ldots (5)$

https://doi.org/10.1017/S0001924000004413 Published online by Cambridge University Press

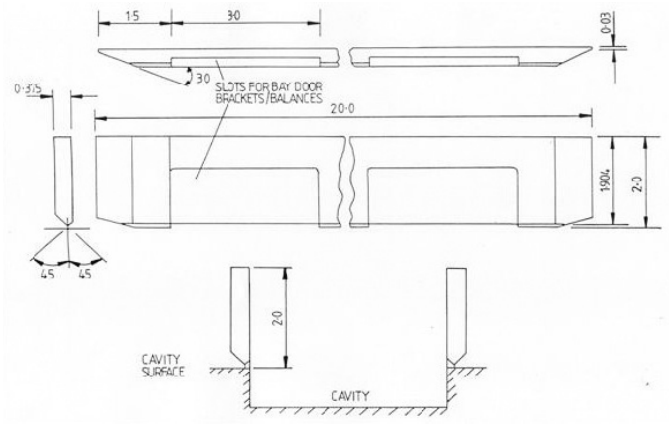

(a) Cavity geometry

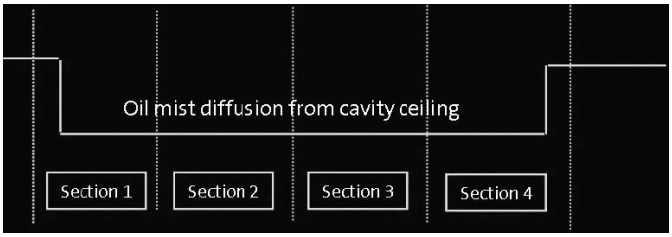

(b) PIV experiment

Figure 2. Schematic of the wind tunnel cavity geometry (including the doors-on configuration) and an illustration of the four different sections along cavity for which laser data acquisitions were taken with the PIV experiment.

whereas for DES,

$$\tilde{d} = C_{DES}\Delta \text{ is used} \qquad \ldots (6)$$

where C_{DES} is the DES coefficient and Δ is the metric of the grid size.

In practice, the following is employed

$$\tilde{d} = \min(d, C_{DES}\Delta),\ \Delta = \max(\Delta_x, \Delta_y, \Delta_z)\ \forall \text{ cell} \qquad \ldots (7)$$

although other metric relations are also possible.

2.4 Description of experiments by Ross *et al*

Wind tunnel experiments conducted by Ross[5] at Aircraft Research Association Ltd (ARA) at Bedford, UK, were used for validation. The ARA wind tunnel is a 9 by 8ft. continuous flow, transonic wind tunnel (TWT) with ventilated roof, floor and side walls. Results for the doors-on configuration are compared with the corresponding experimental data (comparisons being made at several locations along the cavity floor as illustrated in Fig. 1). Where 2D cavity results are mentioned, the comparison was made with the 3D cavity experimental case, where the bay doors were open vertically at 90°. The doors prevent any leakage at the cavity edges in the spanwise direction channelling the flow into the cavity. In this configuration, the flow behaves as if it was 2D and is well represented by modelling the cavity as 2D.

The L/D = 5 cavity model (with W/D = 1) measured 20in in length, and 4in in width and depth. In the doors-on configuration, the doors were positioned at the front and rear walls in the z-direction and spanned the entire length of the cavity (see Fig. 2(a)) and measured 0·375 inches width and 2in in height. The generic cavity rig model (designated as Model M219) was positioned at zero incidence and sideslip and the wind tunnel was operated at a Mach number of 0·85 and atmospheric pressure and temperature. Unsteady pressure measurements were registered inside and outside the cavity via Kulite pressure transducers: ten pressure transducers were aligned along the centreline of the floor of the cavity rig, which was offset from the centreline of the actual cavity model (as shown in Fig. 1), two on the flat plate ahead of the cavity, one on the flat plate aft of the cavity, two on the front and rear walls and four on the port side walls[5]. The data were sampled at 6,000Hz using a high-speed digital data acquisition system.

The measured data were presented in terms of sound pressure level (SPL) and power spectral density (PSD) plots. The SPLs are an indication of the intensity of noise generated inside the cavity and can be obtained from the measurements using the following equation

$$SPL(\mathrm{d}B) = 20\mathrm{Log}_{10}\left(\frac{p_{rms}}{2\times 10^{-5}}\right) \qquad \ldots (8)$$

where the p_{rms} is the RMS pressure normalised by the international standard for the minimum audible sound of 2×10^{-5} Pa. Spectral analysis was performed using fast Fourier transform (FFT) to obtain the power spectral density, which presents the RMS pressure versus frequency and is a measure of the frequency content inside the cavity.

Measurements of the cavity flow-field were provided by PIV experiments conducted by Ross[7]. A stereoscopic two-camera system was employed for velocity measurements accompanied with a two-head Nd-YaG laser. Each laser pulse was fired within time intervals of 1μs. Four data acquisitions were taken with each acquisition comprising of two photographic images taken at 1μs intervals. The width of the laser sheet was limited to approximately 5·5in so the total cavity length of 20in was captured in four sections using motorised camera/laser traverse gear (Fig. 2(b)). Seeding was provided by a combination of water droplets sprayed in the settling chamber and vegetable oil mist diffusion from small holes in the cavity floor. Analysis of the data signals was performed by phase-locking onto each peak of signal and introducing a series of delays to synchronise image acquisitions at a particular part of the cycle. A number of acquisitions were then taken and averaged to define the flow-field at that part of the cycle. For highly unsteady flows with multiple cyclic components, it was recognised that phase-locking on any one component does not 'freeze' the flow-field. As highlighted by Ross[7], combined with the highly turbulent background, all aspects of a cavity flow are not likely to be accounted for. For a complete definition of the flow-field with time-dependency, very high-speed image acquisition equipment would be required.

3.0 RESULTS AND DISCUSSION

The grids used in the numerical modelling and simulation of the empty weapons bay modelled as a clean 3D, L/D = 5, W/D = 1 open rectangular cavity are described in Table 1. All dimensions in these grids were scaled with respect to the cavity length. For the DES and LES grids, the far-field length was set to 3·5 times the cavity length so as to minimise any spurious results from acoustic wave reflections. A flat plate 1·5 times the cavity length (as in the experiment) was used ahead of the cavity to allow the oncoming boundary layer to develop naturally. It is possible that the plate length used ahead of the cavity is not long enough and so the boundary layer could develop further. However comparisons with PIV results, as will be demonstrated later, are good at the front of the cavity so the prediction of the oncoming boundary layer must be reasonably adequate. Furthermore, measurement of the boundary layer height for URANS computations was found to be close to the experimental value ($y/L \approx 0{\cdot}02$) and so the length of the plate used was thought to be adequate.

https://doi.org/10.1017/S0001924000004413 Published online by Cambridge University Press

Table 1
Information on the grids used for the clean cavity in both doors-on and doors-off configurations

Grid type	Pts in cavity (Overall)	Wall-spacing	Blocks in cavity (overall)
		2D cavity	
Coarse	10,302 (33,250)	$1{\cdot}05 \times 10^{-5}$ ($y^+ \approx 0{\cdot}02$)	1 (6)
		Clean cavity with doors-on (90°)	
3D URANS	446,824 (1,483,173)	$1{\cdot}0 \times 10^{-5}$ ($y^+ \approx 0.02$)	20 (110)
3D LES/DES (coarse)	179,520 (1,248,544)	$3{\cdot}125 \times 10^{-3}$ ($y^+ \approx 6$)	64 (240)
3D LES/DES (medium)	493,679 (2,178,480)	$3{\cdot}125 \times 10^{-3}$ ($y^+ \approx 6$)	64 (240)
3D LES/DES (fine)	1,177,646 (4,783,672)	$7{\cdot}1825 \times 10^{-4}$ ($y^+ \approx 1{\cdot}5$)	64 (240)
		Clean cavity with doors-off (90°)	
3D URANS	305,424 (1,174,824)	$2{\cdot}214 \times 10^{-5}$ ($y^+ \approx 0{\cdot}04$)	20 (110)
3D LES/DES (coarse)	179,520 (1,225,824)	$3{\cdot}125 \times 10^{-3}$ ($y^+ \approx 6$)	64 (256)
3D LES/DES (medium)	493,679 (2,178,480)	$3{\cdot}125 \times 10^{-3}$ ($y^+ \approx 6$)	64 (256)
3D LES/DES (fine)	1,177,646 (4,696,128)	$7{\cdot}1825 \times 10^{-4}$ ($y^+ \approx 1{\cdot}5$)	64 (256)
3D LES/DES (very fine)	2,097,152 (8,388,608)	5×10^{-5} ($y^+ \approx 0{\cdot}1$)	64 (256)

Three different grid densities were used for the doors-on computations and four for the doors-off computations (see Table 1). Although points were not doubled in all directions, in order to reduce the computational overhead, the finest grid used for the doors-on case was about 4·8m points (about four times finer than the coarsest level) and about 8·4m points for the doors-off case (about seven times finer than the coarsest level). Where possible, the cell aspect ratio was kept close to unity to minimise the numerical dissipation introduced by the scheme. Grid refinement was dictated by the number of points required to achieve unit cell aspect ratio. For instance, the coarse grid had a coarse wall-spacing of $3{\cdot}125 \times 10^{-3}$ (or $y^+ \approx 8$). For the $L/D = 5$ cavity, 64 cells were applied along the cavity depth to give unit cell aspect ratio in that direction. Resolution in the spanwise and streamwise directions was coarser. To obtain the medium grid level, points were therefore added inside the cavity so as to improve the cell aspect resolution in only the spanwise and streamwise directions. The number of cells in the spanwise direction was increased by a factor of approximately 2·5 to obtain 64 cells along the cavity width and thereby achieving unit cell aspect ratio in this direction. The increase in number of points in the streamwise direction was however much smaller (about only 1·2). For the finer grids, the wall-spacing value was reduced with the aim of resolving the near-wall features better.

In an attempt to minimise the computational overhead in running LES, the Reynolds number was reduced from the experimental Reynolds number of 6·783m to 1m. Preliminary studies into the effects of the Reynolds number were conducted for the 3D, $L/D = 5$, clean cavity (with doors-off) using LES on a coarse grid of 1m points. Two calculations were run: one with the normal Reynolds number of 6·783m and another with a reduced value of 1m. SPLs and PSD (at $x/L = 0{\cdot}95$) are shown in Fig. 3. Little variation in noise levels and frequency content (at $x/L = 0{\cdot}95$) was observed between the two Reynolds numbers.

Rizzetta[3] also conducted his numerical simulations at a lower Reynolds number and still compared his results with experiments using the actual Reynolds number. Furthermore, the effect of

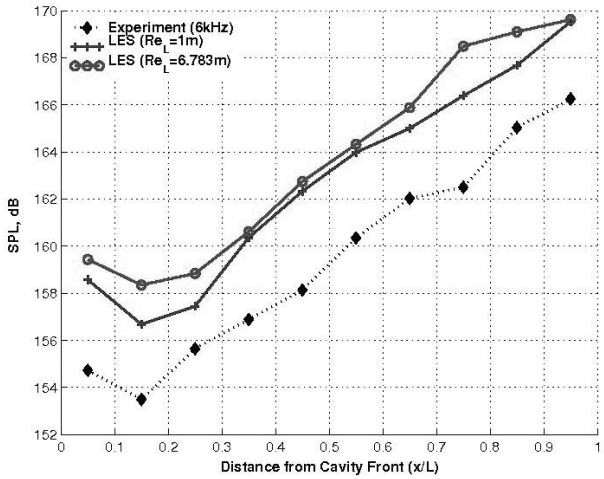

(a) SPLs

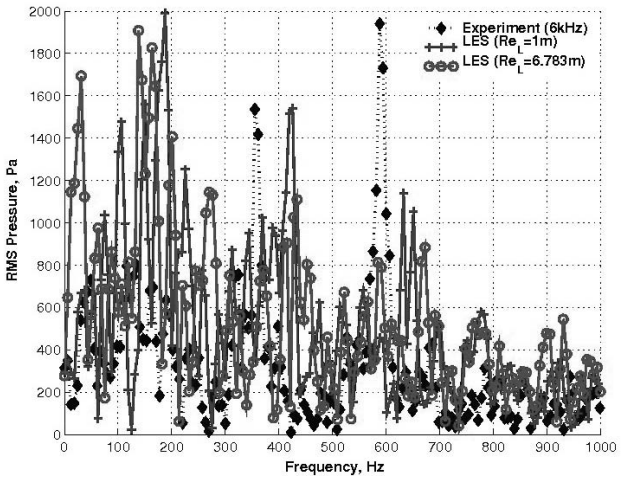

(b) PSD ($x/L = 0{\cdot}95$)

Figure 3. Reynolds number effects on the SPLs and PSD (at $x/L = 0{\cdot}95$) for the 3D, $L/D = 5$, $W/D = 1$ clean cavity (with doors-off) using LES (Smagorinsky SGS).

https://doi.org/10.1017/S0001924000004413 Published online by Cambridge University Press

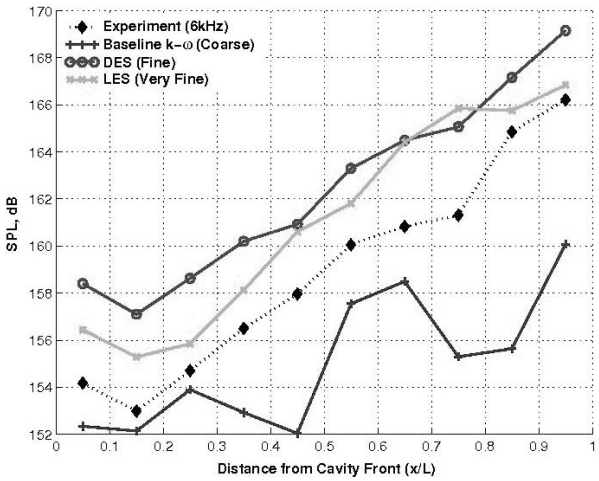

(a) SPLs

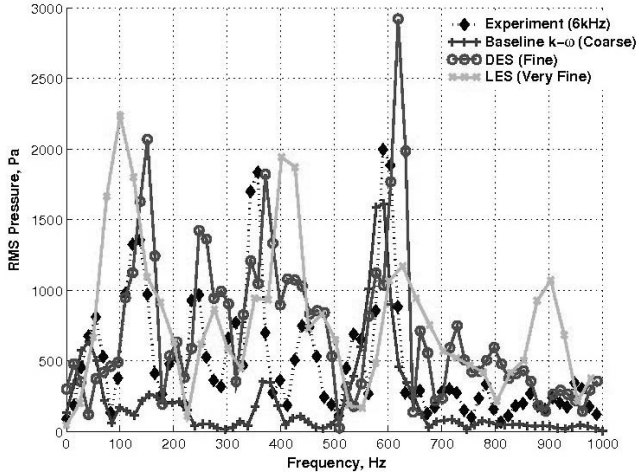

(b) PSD (x/L = 0·95)

Figure 4. SPL and PSD plots (at x/L = 0·95) for the 3D, L/D = 5, W/D = 1 clean cavity with doors-off using the coarse grid for URANS (Menter's baseline k-ω), fine grid for DES-SA and very fine grid for LES (Smagorinsky SGS). Plots taken at z/W = 0·25 and along the cavity floor (y/D = 1).

Reynolds number on cavity flows was also studied by Ross[9]. Although Ross conducted the study at higher Mach numbers, his experiments revealed the effects of Reynolds number to be negligible. Based on these results, all numerical simulations using LES and DES were run at a lower Reynolds number of 1m but still compared with the 6·783m Reynolds number experimental results.

3.1 Doors-off results

Comparisons from the clean, doors-off cavity for the URANS, DES and LES methods with experimental unsteady pressure measurements revealed best agreement between DES and LES and experiment (Fig. 4(a)). URANS results were obtained with the coarse grid (of about 1·5m points) with Menter's baseline k-ω model[8]. A dimensionless time-step of 0·01 (≡1·814 × 10^{-5}s) was used for this computation, with details of the grid used provided in Table 1. The fine grid (comprising about 4·8m points) was used for the DES computation with a time-step of 0·001 (≡1·814 × 10^{-6}s) and the very fine grid (comprising about 8·4m points) for the LES computation with the same time-step. The experimental signal was sampled at 6kHz so the numerical results were sampled at the same rate for proper comparison.

The reason for using a coarser grid for DES computations can be described using Table 2, which compares the run-times for URANS, DES and LES computations. For the same grid, same time-step DES was found to require approximately an order of magnitude less pseudo-steps per time-step. With DES-SA calculations also using an additional equation to solve the flow equations as compared to LES calculations, it can be argued that fewer grid points are required to a achieve similar accuracy to LES calculations. Table 2 also highlights that although LES/DES is cheaper per time-step, it requires more CPU hours and hence is overall more expensive.

The shape of the SPL curve with Menter's baseline k-ω model still resembles the W shape (Fig. 4(a)) that is characteristic of the doors-on case, which will be discussed in greater detail in the following section (Fig. 8(a)). The effect of the doors is to prevent any leakage in the spanwise direction and channels the flow into the cavity making it behave in a more 2D manner. Without doors, however, the flow inside and outside of the cavity is less restricted to move in the spanwise direction. The fact that Menter's baseline k-ω model predicts a completely incorrect SPL shape (unlike LES and DES) suggests that it has difficulty in accommodating effects of the greater transport and redistribution of energy and momentum in the spanwise direction. The greater movement in flow in the spanwise direction also allows smaller structures with a higher frequency content to be created. Evidence of this is shown in the PSD plots in Fig. 4(b), which indicates a strong presence of the 600Hz acoustic tone, i.e. the third Rossiter mode.

Table 2
URANS, DES and LES calculation details

Calculation details	URANS	DES-SA	LES
Cavity configuration	Doors-on	Doors-on	Doors-off
Grid size	1·5 × 10^6	4·5 × 10^6	8·5 × 10^6
Processors	19	320	256
CFD time-step	1·81 × 10^{-5}	1·81 × 10^{-6}	1·81 × 10^{-6}
Unsteady tolerance	0·005	0·001	0·001
Pseudo-steps/CFD time-step	39	6	7
CFD time-steps/min.	0·425	9·72	2·57
Total CFD time-steps	5,506	50,200	18,546
Total CPU hours	3,121	28,100	39,936
Signal duration	0·1s	0·1s	0·034s
Total run-time	9 days	3·46 days	6 days

https://doi.org/10.1017/S0001924000004413 Published online by Cambridge University Press

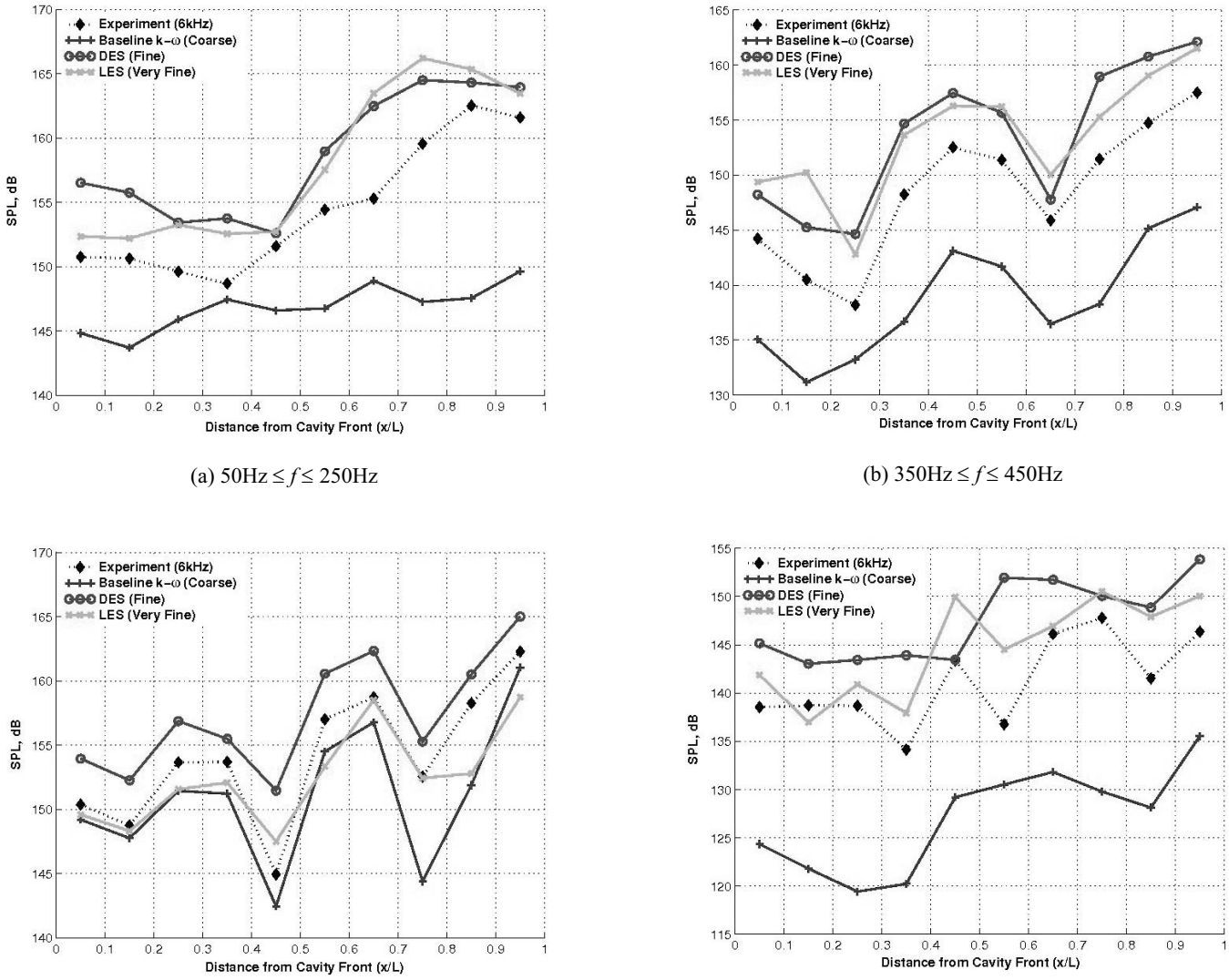

(a) 50Hz ≤ f ≤ 250Hz

(b) 350Hz ≤ f ≤ 450Hz

(c) 500Hz ≤ f ≤ 600Hz

(d) 750Hz ≤ f ≤ 850Hz

Figure 5. Band-limited SPLs for the 3D, L/D = 5, W/D = 1 clean cavity with doors-off using the coarse grid for URANS (Menter's baseline k-ω), fine grid for DES-SA and very fine grid for LES (Smagorinsky SGS). Plots taken at z/W = 0·25 and along the cavity floor (y/D = 1).

A closer inspection of the frequency spectrum can be analysed by looking at band-limited SPL plots, as shown in Fig. 5. This shows the energy content within a particular frequency range and helps to highlight which frequencies are more dominant and so identifies which frequencies play a more significant role in driving the cavity flow. When comparing different numerical methods, as is the case here, this type of analysis is again very useful. Four frequency ranges are plotted in Fig. 5: 50Hz ≤ f ≤ 250Hz (which contains the first Rossiter mode (≈160Hz)), 350Hz ≤ f ≤ 450Hz (which contains the second mode (≈380Hz)), 500Hz ≤ f ≤ 700Hz (which contains the third mode (≈600Hz)) and 750Hz ≤ f ≤ 850Hz (which contains the fourth mode (≈820Hz)). As can be seen in Fig. 5, the third Rossiter mode (≈600Hz) is the most dominant mode for the doors-off cavity case compared to the second mode (≈380Hz) for the doors-on case, as will be shown later. Although Menter's baseline k-ω model predicts the third mode relatively well, it fails to account for either the lower or higher frequencies. In contrast, DES and LES predict the shape of the SPL curves and the level of noise across all the four frequency ranges much better.

Instantaneous Mach contours for both Menter's baseline k-ω model and DES (with the one-equation Spalart-Allmaras model) along the cavity centreline are illustrated in Fig. 6. The Mach number plots divide the lower-velocity (darker (blue)) regions inside the cavity from the transonic (lighter (yellow)) regions outside the cavity. Where these two regions meet is where the shear layer is located. Menter's Baseline k-ω model always predicts a large single primary vortex structure at the cavity rear with some combination of two or more counter-rotating vortices at the cavity front. The shear layer is also consistently found to span the cavity length with a noticeable deflection at the cavity rear (Fig. 6). It is this dual-vortex cycle inside the cavity that results in the W-shaped SPL curve in Fig. 4(a). The difference between the DES and the linear baseline k-ω eddy viscosity model flow-field results lies in the behaviour of the shear layer and this is evident in Fig. 6. At no point for the DES computations does the shear layer extend across the entire length of the cavity. At the most, the shear layer can be observed to be coherent up to the middle of the cavity at which point, if not earlier, it breaks down. What follows is intensive mixing and spreading of

https://doi.org/10.1017/S0001924000004413 Published online by Cambridge University Press

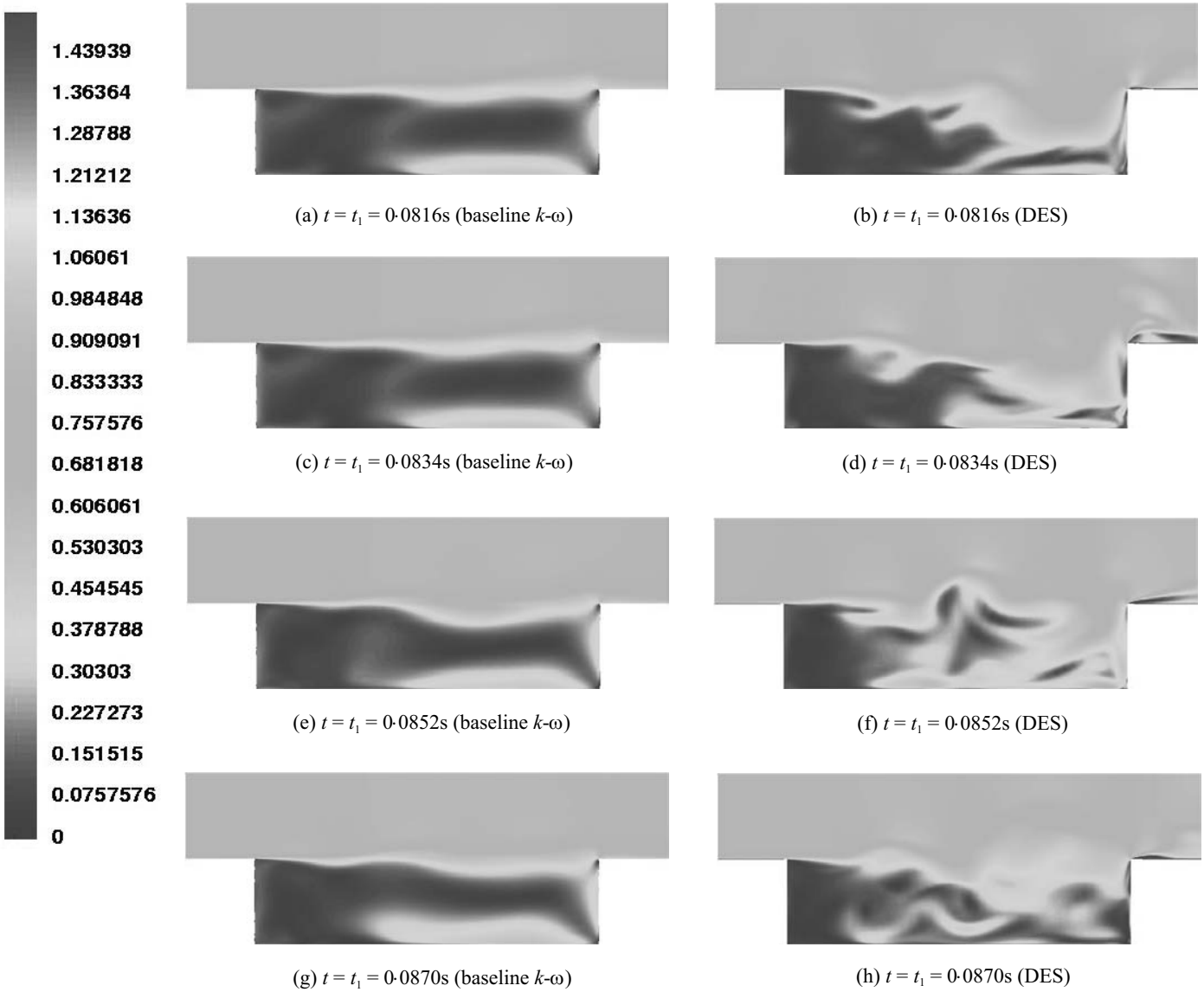

(a) $t = t_1 = 0{\cdot}0816$s (baseline k-ω) (b) $t = t_1 = 0{\cdot}0816$s (DES)

(c) $t = t_1 = 0{\cdot}0834$s (baseline k-ω) (d) $t = t_1 = 0{\cdot}0834$s (DES)

(e) $t = t_1 = 0{\cdot}0852$s (baseline k-ω) (f) $t = t_1 = 0{\cdot}0852$s (DES)

(g) $t = t_1 = 0{\cdot}0870$s (baseline k-ω) (h) $t = t_1 = 0{\cdot}0870$s (DES)

Figure 6. Instantaneous Mach contours for the clean cavity with doors-off illustrating flow features inside the 3D cavity at four different time-steps during flow cycle for the coarse URANS (Menter's baseline k-ω) and fine DES (one-equation Spalart-Allmaras) computations. Plots taken along the cavity centreline ($z/W = 0{\cdot}5$).

the energy from the shear layer and the free-stream with the lower-velocity flow region inside the cavity. The pressure at the cavity rear rises due to this mixing process and is manifested in the form of a rising SPL curve (Fig. 4(a)).

With the shear layer detached, the flow within the cavity is no longer entrained within it and large vortical structures can no longer be sustained. More turbulence, higher frequencies and smaller vortices instead form. These interact with the cavity walls to create regions of higher pressure and more flow activity. Not confined by the shear layer, the flow can now be observed to `spill' over the cavity in both the streamwise and spanwise directions. Indications of these 'spillages' can clearly be seen in LES and, to a lesser extent, in DES computations in Fig. 7, which provides a three-dimensional perspective of the instantaneous flow-field (using Mach contours normalised by the free-stream Mach number of 0·85) inside the 3D clean cavity in the doors-off case. As the linear eddy viscosity model does not predict the breakdown of the shear layer, these vortical `spillages' are also not observed in these computations.

3.2 Doors-on results

Figure 8 shows the difference between the DES, LES and URANS methods in the prediction of noise levels and frequencies for the clean, doors-on cavity configuration. The coarse grid (consisting of about 1·25m points) was used with Menter's baseline k-ω model for URANS computations with a time-step of 0·01 ($1{\cdot}814 \times 10^{-5}$s), the fine grid (containing about 4.8m points) for the DES computation with a time-step of 0·001 ($\equiv 1{\cdot}814 \times 10^{-6}$s) and the medium grid (containing about 2·2m points) for the LES computation with a time-step of 0·005 ($\equiv 9{\cdot}07 \times 10^{-6}$ s). Due to the success of the DES with the one-equation Spalart-Allmaras turbulence model for the doors-off case, it was decided to run a fine grid computation using DES rather than using very fine grids with LES. Two sets of unsteady pressure experimental data were available for the doors-on case: one was sampled at 6kHz and another with a higher sampling rate of 31·25 kHz. Both of these experimental data sets are included in Fig. 8 to emphasise the importance of high resolution experimental data. All numerical results were sampled at 31·25kHz.

https://doi.org/10.1017/S0001924000004413 Published online by Cambridge University Press

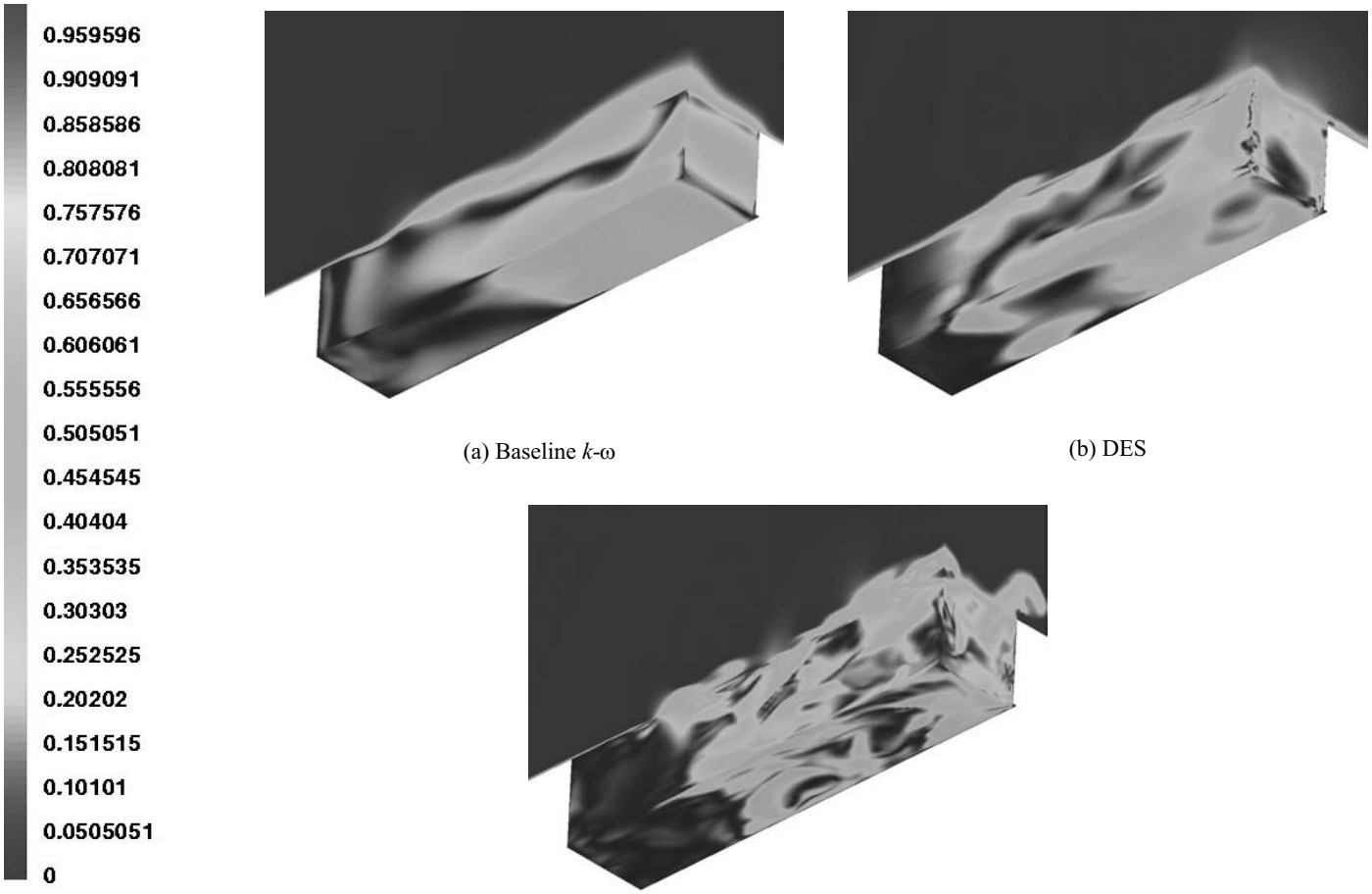

(a) Baseline k-ω (b) DES

(c) LES

Figure 7. Three-dimensional perspective of the flow-field inside the 3D, L/D = 5 clean cavity with doors-off for the URANS (Menter's Baseline k-ω), DES (one-equation Spalart-Allmaras) and LES (standard Smagorinsky SGS) methods. Plots show instantaneous Mach contours normalised by the free-stream Mach number of 0·85.

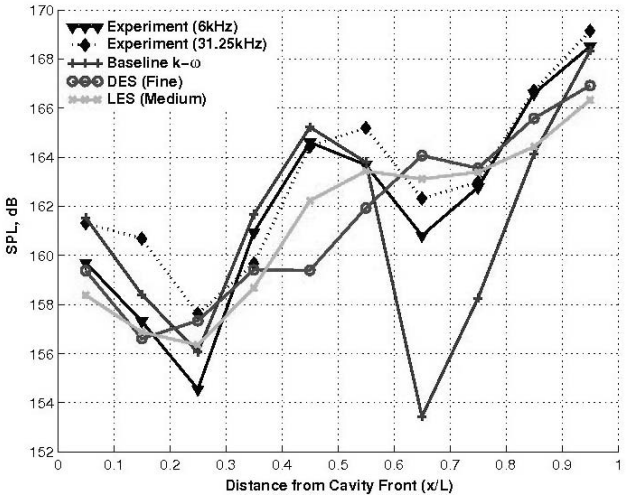

(a) SPLs

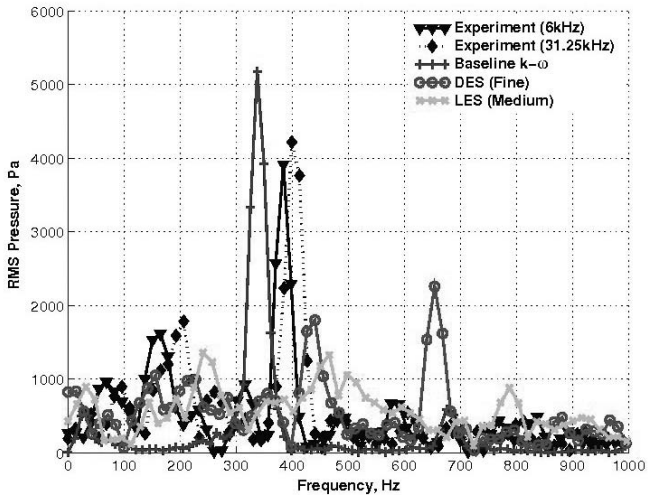

(b) PSD (x/L = 0·95)

Figure 8. SPL and PSD plots (at x/L = 0·95) for the 3D, L/D = 5, W/D = 1 clean cavity with doors-on (at 90° vertically) using the coarse grid for URANS (Menter's bBaseline k-ω), fine grid for DES-SA and medium grid for LES (Smagorinsky SGS). Plots taken at z/W = 0·25 and along the cavity floor (y/D = 1).

https://doi.org/10.1017/S0001924000004413 Published online by Cambridge University Press

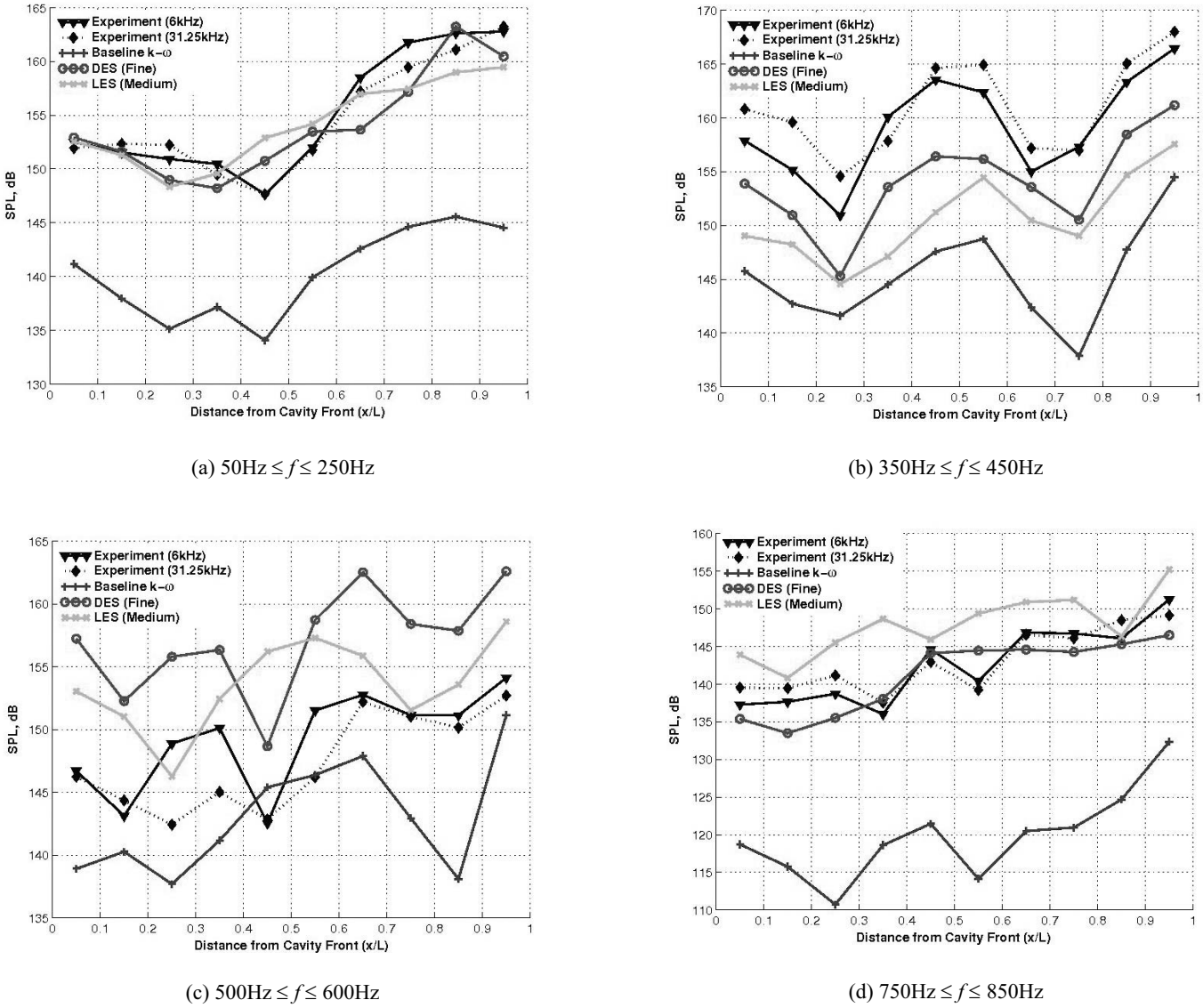

(a) 50Hz ≤ *f* ≤ 250Hz

(b) 350Hz ≤ *f* ≤ 450Hz

(c) 500Hz ≤ *f* ≤ 600Hz

(d) 750Hz ≤ *f* ≤ 850Hz

Figure 9. Band-limited SPLs for the 3D, *L*/*D* = 5, *W*/*D* = 1 clean cavity with doors-on (at 90° vertically) using the coarse grid for URANS (Menter's Baseline *k*-ω), fine grid for DES-SA and very fine grid for LES (Smagorinsky SGS). Plots taken at *z*/*W* = 0·25 and along the cavity floor (*y*/D = 1).

Menter's baseline *k*-ω turbulence model was used for URANS while the one-equation Spalart-Allmaras model was used with DES to realise the turbulent near-wall properties. Variations in SPLs across the cavity length on its floor are illustrated in Fig. 8(a). All three methods agree reasonably well with experiment, with the linear baseline *k*-ω model results agreeing even better with experiment in some cases. Near the front of the cavity, for instance, the shape of the SPL curve for Menter's baseline *k*-ω model follows the experiment better than the DES and LES counterparts.

A closer inspection of the frequency content is again provided using band-limited SPL plots in Fig. 9. This illustrates that the agreement between Menter's Baseline *k*-ω model and experiment is not as satisfactory as previously thought. Neither the first (≈160Hz in Fig. 9(a)) nor the third (≈600Hz in Fig. 9(c)) Rossiter modes are captured. The second Rossiter mode (≈380Hz in Fig. 9(b)) is well captured but is over-predicted by about 1kPa. This over-prediction was found to be a common occurrence for comparisons of most linear two-equation eddy viscosity results with experiments.

3.3 Comparisons against PIV data

PIV data were provided by Ross[7], as described previously. The PIV experiment was conducted for the 3D cavity in the doors-on configuration only and so results from the corresponding doors-on computations are only compared with it.

Time-averaged streamwise velocity profiles for three different stations inside the cavity (x/L = 0·05, x/L = 0·55 and x/L = 0·95 — see Fig. 1 for the positions of these pressure taps) for both DES-SA (with the fine grid) and LES (with the medium grid) computations are illustrated in Fig. 10. The black line denotes the PIV results. Velocity profiles with the best available URANS results, i.e. results from the linear SST eddy viscosity model for the 2D cavity grid, which as described before is a good representation of the 3D cavity with doors-on, are also shown. Details of the grids used are presented in Table 1. A dimensionless time-step of 0·01 (≡1·814 × 10^{-5}s) was used for the 2D computation, 0·001 (≡1·814 × 10^{-6}s) for the DES computation and 0·005 (≡9·07 x 10^{-6}s) for the LES calculation.

https://doi.org/10.1017/S0001924000004413 Published online by Cambridge University Press

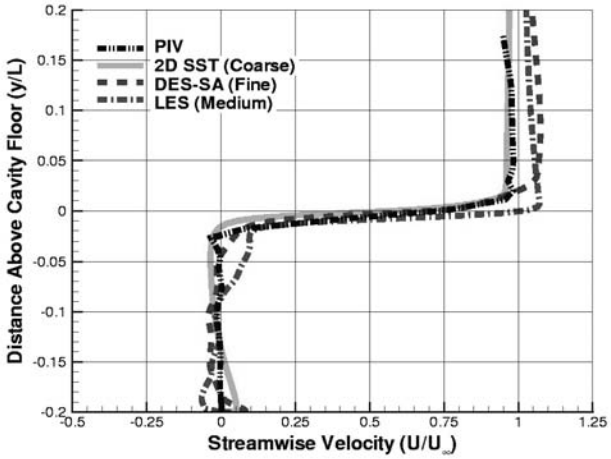

(a) U-velocity ($x/L = 0{\cdot}05$)

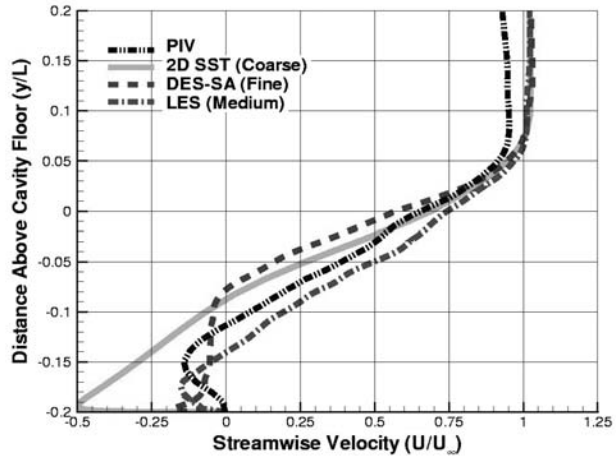

(b) U-velocity ($x/L = 0{\cdot}55$)

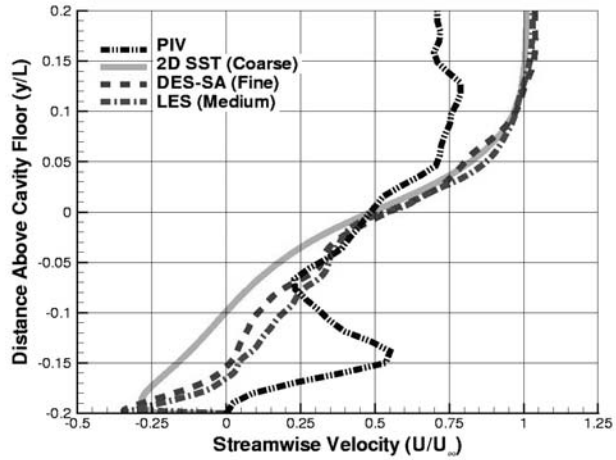

(c) U-velocity ($x/L = 0{\cdot}95$)

Figure 10. Time-averaged streamwise (U/U_∞) velocity profiles for the clean cavity with doors-on along cavity floor at $x/L = 0{\cdot}05$, $x/L = 0{\cdot}55$ and $x/L = 0{\cdot}95$ using 2D URANS coarse grid (with SST model (solid, green)), fine DES grid (with Spalart-Allmaras (dashed, red)) and medium LES grid (dashed-dot blue). Black line corresponds to experimental PIV data (provided by Ross[7]).

At the first station, i.e. $x/L = 0{\cdot}05$, the agreement between DES, LES and PIV is good. Even the 2D results match the PIV measurements well at this position. The reason for this good agreement with all three numerical methods and PIV may be due to the fact that flow activity at this position is not as strong as in other parts of the cavity. Once the flow separates at the cavity lip, the momentum that is imparted from the boundary layer into the resulting shear layer keeps it coherent and prevents it from breaking up immediately. As the turbulent stresses and diffusion begin to take effect, the shear layer begins to redistribute its energy into the cavity. If energy is not fed back into the shear layer, for instance, via the vortical structures, then the shear layer will eventually break up, as was realised for the doors-off case described before. For the doors-on case, however, because the doors minimise the flow activity in the spanwise direction, energy that would otherwise normally be redistributed into the spanwise direction is transferred into the x-y plane, allowing the vortices inside the doors-on cavity to be stronger. More energy is fed back into the shear layer, which in turn allows it to extend across a greater proportion of the cavity length. These processes mean that energy from the shear layer is transferred into the cavity further downstream for the doors-on cavity and as a result flow activity at the cavity front can be significantly less. Evidence of this is present in Fig. 10(a), where the variation in the streamwise velocity profile is almost negligible. With the flow less unsteady here and higher frequencies absent, the linear SST model predicts the velocity profiles as well as DES and LES.

At the cavity middle, i.e. $x/L = 0{\cdot}55$, better agreement was obtained with DES and LES. Results with the linear SST model for the 2D cavity showed a larger variation in the streamwise velocities indicating that strength of the primary vortex is over-predicted. At the cavity rear ($x/L = 0{\cdot}95$), agreement with even DES, LES and PIV deteriorates. Explanation for this may lie in the manner in which the PIV experiment was conducted. As mentioned previously, the laser used for the PIV experiment had a width of approximately 5·5in, which is roughly equivalent to a quarter of the cavity length. The laser was fired at four different sections in order to cover the entire length of the cavity (Fig. 2(b)). The resolution of the PIV experiment was found to be good at the first two stations the computational results were analysed at, i.e. at $x/L = 0{\cdot}05$ and $x/L = 0{\cdot}55$, but was not equally good at the third station, i.e. at $x/L = 0{\cdot}95$. This is illustrated in Fig. 11, which indicates the variations in the streamwise and transverse velocity components along the length of the cavity for the PIV experiment at a distance equal to the depth of the cavity above the cavity lip.

The experiment was conducted at a Mach number of 0·85 and a freestream velocity of 296ms^{-1}. In sections 1 and 3 of the PIV experiment, which are where the first two stations, $x/L = 0{\cdot}05$ and $x/L = 0{\cdot}55$, lie respectively, resolution of the experiment is good and the streamwise velocity is close to its anticipated freestream value of 296ms^{-1} (Fig. 11(a)). In section 4, however, which is where the third station ($x/L = 0{\cdot}95$) lies, the resolution deteriorates and the streamwise fluctuations are significantly larger. A consistent story is told by the transverse streamwise plots in Fig. 11(b). This possibly explains the discrepancies between the LES, DES and PIV data at the cavity rear. This also further emphasises the problems with using PIV for highly unsteady flows at high Mach and Reynolds numbers. As mentioned by Ross[7], higher imaging and data acquisition equipment is likely to be required for consistently good resolution throughout the cavity cross-section.

https://doi.org/10.1017/S0001924000004413 Published online by Cambridge University Press

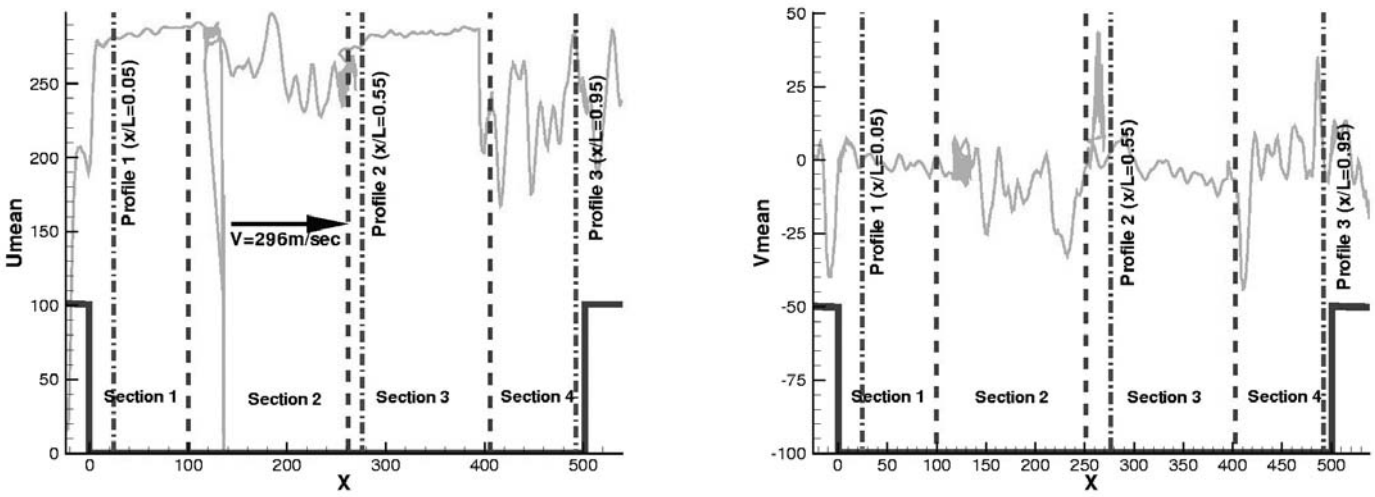

(a) PIV streamwise (U) velocity

(b) PIV transverse (V) velocity

Figure 11. Streamwise and transverse velocity traces at a distance equal to the depth of the cavity above the cavity lip for the PIV experiment.

4.0 CONCLUSIONS

Analysis of weapon bay flow modelled by a 3D cavity with L/D = 5 and W/D = 1 was presented. All computations were conducted at a free-stream Mach of 0·85 and a Reynolds number of 6·783m using the PMB code developed by University of Glasgow. Analysis of clean weapon bays is presented where results from URANS, LES and DES are compared. Menter's Baseline k-ω linear eddy viscosity model was selected for URANS computations as this was found to be the most accurate and robust turbulence model out of all others tested. The standard Smagorinsky SGS was used for LES and the one-equation Spalart-Allmaras model was used for DES computations for both doors-off and doors-on configurations.

Analysis of unsteady pressure measurements with experiment revealed that both DES and LES consistently gave better agreement than the baseline k-ω model in terms of frequency content, phase and noise levels for both the doors-on and doors-off configurations. DES SPLs were on average within 3-4 with doors-off and within 1-5dB with doors-on from experiment while LES results were mostly within 1-2dB for both configurations. The linear baseline k-ω model had difficulty in capturing most of the higher (and in some cases, some of the lower) frequencies in both cases. For the doors-off case, the linear baseline k-ω model still predicted a W-shaped SPL curve as it did for the doors-on case unlike LES and DES, which correctly predicted the shape of the SPL curve. Flow-field visualisation for the doors-off cavity with the linear baseline k-ω model and DES revealed that DES predicted a breakdown of the shear layer while the linear baseline k-ω model consistently illustrated a coherent shear layer that spanned the cavity. It was concluded that the two-equation k-ω linear eddy viscosity model had difficulty in accounting for the larger transport and/or diffusion of energy and momentum present in the doors-off case.

For the doors-on case, a first glance of the SPLs revealed that the baseline k-ω model provided the best agreement with experiments (with SPL differences even less than 1-2dB at the front of the cavity). A closer inspection of the results (through band-limited frequency analysis) however revealed that the URANS model predicted the dominant mode (≈380Hz) within 1kPa but again failed to account for the frequencies lower and higher than the dominant mode. In contrast both LES and DES fared much better.

Streamwise velocity plots were compared for the doors-on case with PIV measurements and showed consistently good agreement at the cavity front and middle (within 15-20% for DES and within 10% for LES) for different DES variants and LES. At the cavity rear, the agreement with PIV deteriorated and these discrepancies may be attributed to poor resolution in the PIV experiment at this position.

Overall, the obtained results highlight the potential of DES and LES for such unsteady, massively separated flows. Although expensive, DES and LES appear to be consistent in their predictions and captured the correct energy distribution between the cavity flow modes. At present, work is directed towards exploiting the good predictive capabilities of DES and LES to assess possible control methods for cavity flows. From a turbulence modelling perspective, the use of more sophisticated eddy viscosity models or second-moment closure models may predict the cavity flow behaviour more accurately. This however requires further investigation.

ACKNOWLEDGEMENTS

The work detailed in this paper was supported by both BAE Systems and the Engineering and Physical Sciences Research Council (EPSRC). The authors would like to extend their gratitude to Dr John Ross and Dr Graham Foster of QinetiQ (Bedford) for providing the experimental data and to Dr David Kirkham of BAE Systems (Farnborough) for the many useful discussions on cavity flows. The HPCx computer time was provided through the UK Applied Aerodynamics Consortium (UKAAC) under EPSRC grant GR/S91130/01.

REFERENCES

1. ROSSITER, J.E. Wind tunnel experiments on the flow over rectangular cavities at subsonic and transonic speeds, October 1967, Royal Aircraft Establishment Report No 64037.
2. STALLINGS, R.L. Store separation from cavities at supersonic flight speeds, *J Spacecraft and Rockets*, March-April 1983, **20**, (2), pp 129-132.
3. RIZZETTA, D.P. and VISBAL, M.R. Large-eddy simulation of supersonic cavity flowfields including flow control, *AIAA*, August 2003, **41**, (8), pp 1438-1443.
4. SPALART, P.R. Strategies for turbulence modelling and simulations, *Int J of Heat and Fluid Flow*, June 2000, **21**, (3), pp 252-263.
5. ROSS, J.A. and PETO, J.W. The effect of cavity shaping front spoilers and ceiling bleed on loads acting on stores, and on the unsteady environment within weapon bays, QinetiQ report, March 1997.
6. BADCOCK, K.J., RICHARDS, B.E. and WOODGATE, M.A. Elements of computational fluid dynamics on block structured grids using implicit solvers, *Progress in Aerospace Sciences*, 2000, **36**, pp 351-392.
7. ROSS, J.A. PIV measurements of the flowfields in an aerodynamically deep cavity, May 2002, private communication.
8. MENTER, F.R. Two-equation eddy-viscosity turbulence models for engineering applications, *AIAA*, August 1994, **32**, (8), pp 1598-1605.
9. ROSS, J.A. Cavity acoustic measurements at high speeds, March 2000, QinetiQ report DERA/MSS/MSFC2/TR000173.

https://doi.org/10.1017/S0001924000004413 Published online by Cambridge University Press